Mesoscale Predictability of Moist Baroclinic Waves: Convection-Permitting Experiments and Multistage Error Growth Dynamics

FUQING ZHANG AND NAIFANG BEI

Department of Atmospheric Sciences, Texas A&M University, College Station, Texas

RICHARD ROTUNNO AND CHRIS SNYDER

National Center for Atmospheric Research,* Boulder, Colorado

CRAIG C. EPIFANIO

Department of Atmospheric Sciences, Texas A&M University, College Station, Texas

ABSTRACT

A recent study examined the predictability of an idealized baroclinic wave amplifying in a conditionally unstable atmosphere through numerical simulations with parameterized moist convection. It was demonstrated that with the effect of moisture included, the error starting from small random noise is characterized by upscale growth in the short-term (0–36 h) forecast of a growing synoptic-scale disturbance. The current study seeks to explore further the mesoscale error-growth dynamics in idealized moist baroclinic waves through convection-permitting experiments with model grid increments down to 3.3 km. These experiments suggest the following three-stage error-growth model: in the initial stage, the errors grow from small-scale convective instability and then quickly $[O(1\ \mathrm{h})]$ saturate at the convective scales. In the second stage, the character of the errors changes from that of convective-scale unbalanced motions to one more closely related to large-scale balanced motions. That is, some of the error from convective scales is retained in the balanced motions, while the rest is radiated away in the form of gravity waves. In the final stage, the large-scale (balanced) components of the errors grow with the background baroclinic instability. Through examination of the error-energy budget, it is found that buoyancy production due mostly to moist convection is comparable to shear production (nonlinear velocity advection). It is found that turning off latent heating not only dramatically decreases buoyancy production, but also reduces shear production to less than 20% of its original amplitude.

1. Introduction

Although the synoptic-scale evolution of the typical midlatitude weather system is relatively well forecasted, numerical weather prediction models still have difficulties in forecasting the "mesoscale details" that are of most concern to the typical user of the forecast. It is therefore of great interest to assess the predictability of these mesoscale weather systems, particularly with respect to the amount and spatial distribution of the associated precipitation. The notion of a limit of predictability originated with Lorenz (1969), who suggested that skillful weather forecasts would be limited to a finite lead time even for forecast models and initial conditions of much greater accuracy than presently available. He conjectured that the increasingly rapid error growth would impose an inherent, finite limit to the predictability of the atmosphere, as successive refinements of the initial estimate would yield smaller and smaller increments to the length of a skillful forecast (Lorenz 1969).

Existing demonstrations of the limit of predictability are mostly based on statistical closure models of homogeneous isotropic turbulence (Lorenz 1969; Leith 1971;

Corresponding author address: Dr. Fuqing Zhang, Department of Atmospheric Sciences, Texas A&M University, College Station, TX 77845-3150.
E-mail: fzhang@tamu.edu

Leith and Kraichnan 1972; Metais and Lesieur 1986). These closure models indicate, in agreement with simple dimensional arguments (Lorenz 1969; Lilly 1972), that the energy-cascading inertial range of either two- or three-dimensional turbulence has an intrinsic, finite limit of predictability, while the two-dimensional enstrophy-cascading inertial range does not. Direct numerical simulations provide some support for predictability results from closure models in the two-dimensional enstrophy-cascading range (Lilly 1972; Boffetta et al. 1996). The relevance of any of these calculations to the real atmosphere, however, is uncertain, as those scales are characterized not by homogeneous turbulence but by highly intermittent phenomena such as fronts and organized moist convection.

It remains an open question for mesoscale weather systems whether the predictability limit is a few tens of hours or several days. The initial results of Anthes et al. (1985) indicated that the mesoscale enjoyed enhanced predictability, but their results were subsequently found to arise from the perfectly known lateral boundary conditions they employed (Errico and Baumhefner 1987; Vukicevic and Errico 1990). None of these studies suggested distinct mechanisms for error growth at meso- or smaller scales. Studies by Pielke et al. (1991) and others have suggested that topography and surface properties may control the development of mesoscale features and thus extend their predictability. However, recent results from Nuss and Miller (2001) suggest that topography can limit the predictability of terrain-induced mesoscale precipitation systems when small synoptic-scale errors are introduced.

Most recently, the authors have explored the growth of small-scale differences in simulations of the "surprise" snowstorm of January 2000 (Zhang et al. 2002, 2003). Integrations of a high-resolution regional numerical weather prediction (NWP) model indicate that moist convection is a primary mechanism for forecast-error growth at sufficiently small scales, and that convective-scale errors contaminate the mesoscale within lead times of interest to NWP, thus effectively limiting the predictability of the mesoscale. In an attempt to generalize these results from a single case study, we further studied the error growth in an idealized baroclinic wave amplifying in a conditionally unstable atmosphere (Tan et al. 2004, hereafter TZRS04). The latter experiments with parameterized moist convection show that without the effects of moisture, there is little error growth in the short-term (0–36 h) forecast error (starting from random noise), even though the basic jet used produces a rapidly [$O(1$ day)] growing synoptic-scale disturbance; when the effect of moisture is included, the error is characterized by upscale growth, similar to that found in our studies of the numerical prediction of the "surprise" snowstorm.

The current study seeks to characterize the mesoscale error-growth dynamics in our simulated idealized moist baroclinic waves by using higher-resolution, convection-permitting experiments. It was demonstrated in Zhang et al. (2003) that errors grow faster in higher-resolution convection-permitting simulations with faster upscale transfer of error energy than in experiments with parameterized moist convection. Although the latter results show that moist convection significantly impacts the predictability at the mesoscale, the mechanisms controlling the growth and upscale transfer of forecast errors remain undetermined. The current study seeks to identify the error-growth characteristics and to offer some insight into the prevalent dynamical processes at work.

This paper is organized as follows. The experimental design is described in the next section. Section 3 presents the sensitivity of error growth to model resolution. Section 4 presents an overview of the error growth in several simulations of moist baroclinic waves. These results suggest the three-stage error-growth conceptual model presented in section 5. Further testing of the conceptual model is carried out through the initial-condition and moisture-content sensitivity experiments discussed in section 6. For a more quantitative analysis of the error-growth dynamics we present in section 7 a budget analysis of the error energy. Section 8 contains the summary.

2. Experimental design

The same mesoscale model [fifth-generation Pennsylvania State University–National Center for Atmospheric Research Mesoscale Model (MM5, version 2)] as in TZRS04 is used for this study. However, in addition to the two model domains D1 and D2 with, respectively, the 90- and 30-km horizontal grid increments used in TZRS04, two nested domains D3 and D4 with respective grid increments of 10 and 3.3 km are nested within domain D2 to permit explicit convection (Fig. 1). The model employs Cartesian coordinates and a constant Coriolis parameter. Domain D1 is configured in the shape of a channel 18 000 km long (in the east–west, or x direction) and 8010 km wide (in the north–south, or y direction) while domain D2 is a rectangular subdomain 8400 km long and 4800 km wide centered at (9720 km, 3960 km) within domain D1. The 10-km domain D3 is a rectangular subdomain 5800 km long and 2800 km wide within domain D2 while the 3.3-km domain D4 is 1933 km long and 1333 km wide within domain D3. The planetary boundary layer scheme of
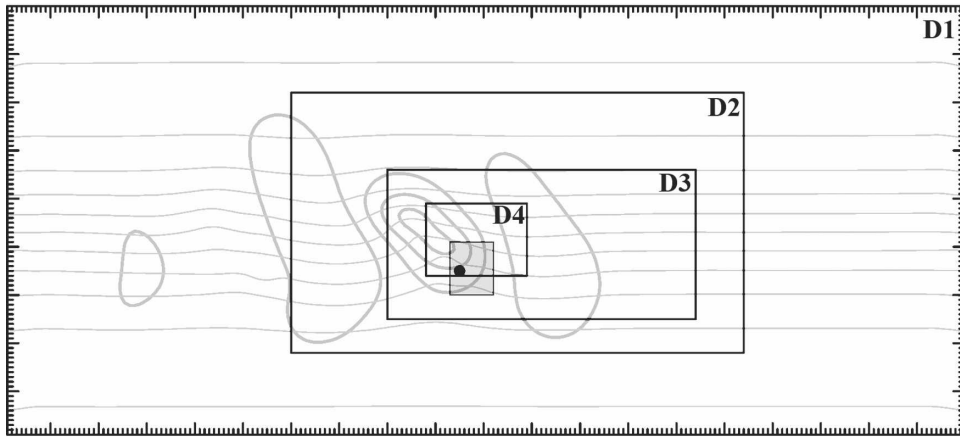
FIG. 1. Configuration of the model domains (D1, D2, D3, and D4). Also shown are the D1 simulated surface potential temperature (thin line, $\Delta = 6$ K) and sea level pressure (thick line, $\Delta = 8$ hPa) valid at 36 h of the coarsest grid forecast, which are the initial conditions for the nested domains. The gray-shaded box denotes the location of the perturbation for experiment "BOX-D3P," and the bold dot denotes the location of the perturbed sounding for experiment "SND-D3P." The distance between small tick marks is 90 km.

Hong and Pan (1996) and the Dudhia (1993) simple ice microphysics scheme are used in all domains. The Grell (1993) cumulus parameterization is used in domains D1 and D2 but no convective parameterization is used in domains D3 and D4. At the lower boundary a drag law (with no topography and a uniform surface roughness length) and zero heat/moisture flux are applied in all domains.

The same initial conditions as used in TZRS04 are employed for this study in which a three-dimensional "balanced" perturbation (Rotunno and Bao 1996, p. 1057) was added at the tropopause level of a two-dimensional baroclinically unstable jet with ample moisture. The coarse domain D1 is integrated for 72 h using the initial conditions described in Fig. 1 of TZRS04 with fixed lateral boundary conditions. This integration with a 90-km grid scale is analogous to a global model forecasting an amplifying, eastward-propagating synoptic-scale disturbance. Experiment CNTL-D3 employs the two nested domains, D2 and D3, initialized at 36 h of the coarse domain D1 forecast with the 10-km grid covering the area where moist processes are active over the subsequent integration. Experiment CNTL-D4 employs the three nested domains D2, D3, and D4; two-way nesting was applied between domains D2 and D3 as well as between domains D3 and D4. The initial and boundary conditions of the nested domains were derived from domain D1; no feedback was allowed from the nested domains. The nested domains may be viewed as a limited-area mesoscale forecast driven by a hemispheric forecast (from domain D1). All nested grids are initialized at the 36-h integration time of domain D1. The sea level pressure (SLP)

and surface potential temperature fields at the time when the nested domains were initiated is also shown in Fig. 1. This is also the time at which the perturbations were introduced.

The same initial condition used in CNTL-D2P of TZRS04 is used to initiate the "identical twin" simulations of CNTL-D3P in which the initial temperature fields of the 30-km grid domain D2 was perturbed with random, Gaussian noise with zero mean and a standard deviation of 0.2 K, which is independent at each grid point; this same initial perturbation is also used for CNTL-D4P. The lateral boundary conditions for the 30-km domain D2 in CNTL-D3P and CNTL-D4P are not perturbed (i.e., they are identical to those of CTRL-D2).

Several additional simulations with different initial perturbations were also performed. CNTL-D3P2 is the same as in CNTL-D3 but a different realization of random perturbations of the same amplitude is used. BOX-D3P uses the same perturbations as in CNTL-D3P but the perturbations are only applied to the small gray-shaded box in Fig. 1, where the model atmosphere becomes moist unstable at $t = 36$ h. SND-D3P is the same as in CNTL-D3P but the random perturbations are only applied to one vertical column of the model grid (i.e., vertical sounding) at the bold dot point shown in Fig. 1.

3. Resolution dependence of the simulated life cycle of moist baroclinic waves

TZRS04 demonstrated that the 90- and 30-km domain simulations (domains D1 and D2; Figs. 2–3 of
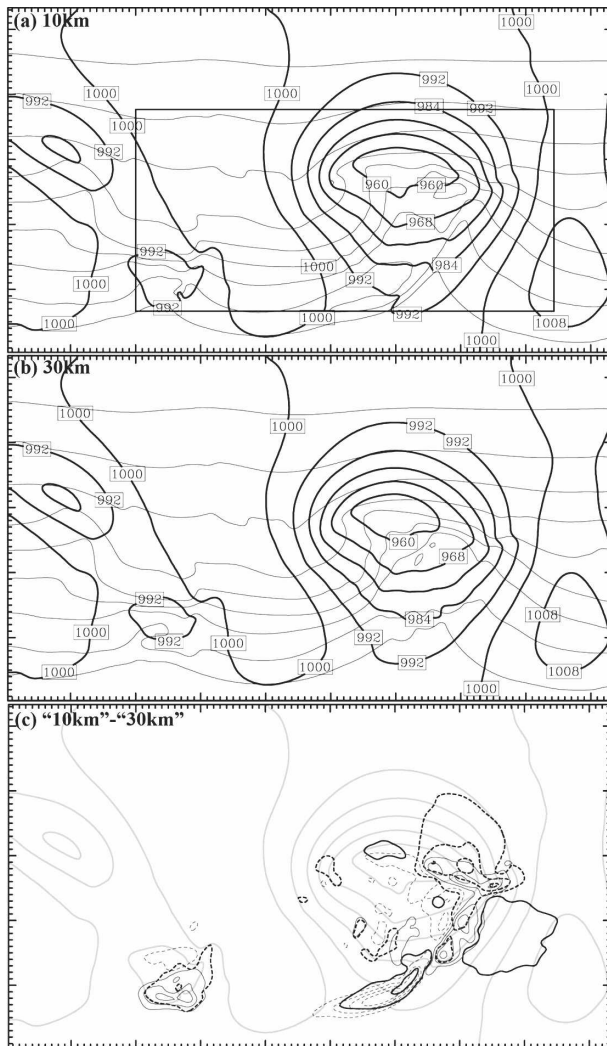
FIG. 2. The surface potential temperature (thin line, $\Delta = 6$ K) and sea level pressure (thick line, $\Delta = 8$ hPa) valid at 36 h of the nested grid forecast simulated by experiments (a) CNTL-D3 (10-km run) and (b) CNTL-D2 (30-km run), both plotted on the 30-km grid. (c) The difference ("CNTL-D3" − "CNTL-D2") of the surface potential temperature (thin line, $\Delta = 2$ K; solid, positive; dashed, negative) and sea level pressure (thick line, $\Delta = 2$ hPa; dashed, negative) along with the sea level pressure from CNTL-D3 (gray line, $\Delta = 8$ hPa). The rectangular box in (a) denotes the location of the 10-km nested domain D3. The distance between tick marks is 90 km.

TZRS04) reproduced fairly realistic features found in past observations and simulations of the life cycle of a typical extratropical cyclone (e.g., Shapiro et al. 1999). However, those simulations were still significantly limited by the model grid resolution and their use of parameterized moist convection. Figure 2 shows that there are substantial differences in the 36-h pressure and temperature simulations at the surface between the 30-km CNTL-D2 simulation with parameterized con-

vection and the present 10-km CNTL-D3 simulation without cumulus parameterization. The difference is especially pronounced in the area of moist processes near the surface frontal zones with a deeper surface cyclone and sharper temperature gradients simulated in CNTL-D3.

Although even higher-resolution simulations are preferred, in this paper we will use the 10-km simulations to examine the influence of moist convection on the mesoscale predictability of extratropical cyclones for the following reasons: 1) our current computational resources do not allow us to perform simulations with the 3.3-km domain covering the area of moist convection for the entire 36-h period; 2) as shown in Fig. 3, the difference of the 9-h simulations between the convection-permitting 3.3-km CNTL-D4 and the convection-permitting 10-km CNTL-D3 (Fig. 3d) is much smaller than the difference between the convection-parameterized 30-km CNTL-D2 and convection-permitting 10-km CNTL-D3 (Fig. 3c; all verified at the same 30-km domain D2 shown); 3) the difference between CNTL-D4 and CNTL-D4P is comparable to the difference between CNTL-D3 and CNTL-D3P after 9 h of integration (see below for more on this). Since both domains D3 and D4 simulate moist processes without cumulus parameterization, we loosely term both the 3.3- and 10-km simulations as *convection-permitting*[1] experiments.

4. Error growth in the convection-permitting simulations of moist baroclinic waves

We begin by examining the evolution of the small initial difference between the two convection-permitting simulations, CNTL-D3 (unperturbed) and CNTL-D3P (perturbed). Figure 4 shows the 500-hPa meridional wind difference δv at 03, 06, 12, 18, 24 and 36 h along with the CNTL-D3 simulated 500-hPa height and the 50 J kg^{-1} m^{-1} contour of convective available potential energy (CAPE). By 3 h, the maximum wind difference $\delta v_{max} \approx 7$ m s^{-1} and is concentrated in the CAPE ridge on the southeast side of the upper trough (Fig. 4a). At this time, as in TZRS04, the initial random disturbance added to the temperature field has decayed everywhere except for a small region in the southeast quadrant of the upper trough and surface cyclone (not

---

[1] Convection-resolving experiments would require a grid scale well within the inertial subrange of moist cumulus convection (see e.g., Bryan et al. 2003). By convection-permitting resolution it is understood that the basic nonhydrostatic dynamics of a convective cell is captured, but that smaller-scale turbulent mixing associated with the cloud is not.
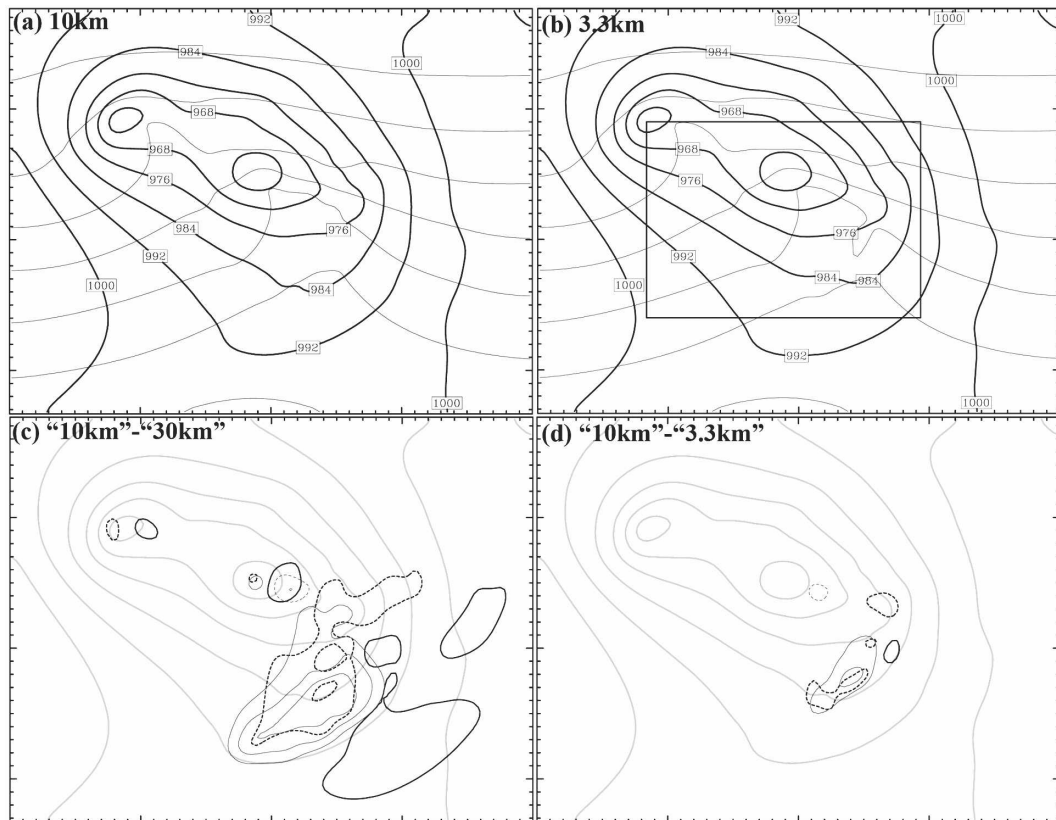
FIG. 3. The surface potential temperature (thin line, $\Delta = 6$ K) and sea level pressure (thick line, $\Delta = 8$ hPa) valid at 9 h of the nested grid forecast simulated by experiments (a) CNTL-D3 (10-km run) and (b) CNTL-D4 (3.3-km run), both plotted on a subdomain of the 30-km grid. Also shown are the difference fields for (c) "CNTL-D3" − "CNTL-D2" and (d) "CNTL-D3" − "CNTL-D4" of the surface potential temperature (thin line, $\Delta = 2$ K; dashed, negative) and sea level pressure (thick line, $\Delta = 2$ hPa; dashed, negative) along with the sea level pressure from CNTL-D3 (gray line, $\Delta=8$ hPa). The rectangular box in (b) denotes the location of the 3.3-km nested domain D4. The distance between tick marks is 90 km.

shown). While remaining in a similar location and at a similar spatial scale at 6 h, δv_{max} increases to 20 m s^{-1} (Fig. 4b). Over the next 6 h (Fig. 4c), δv_{max} changes little but the inherent length scales of $\delta v(x, y)$ and areal coverage of significant $|\delta v| > 0$ grow. This trend continues throughout the 36 h of simulation (Figs. 4d–f). The magnitude, horizontal extent, and scales of these differences are much larger than those derived from the 30-km simulations of TZRS04 (see their Fig. 4).

The error growth between CNTL-D3 and CNTL-D3P can be summarized with the time evolution of domain-integrated difference total energy (DTE; solid curve in Fig. 5) and its spectrum analysis (Fig. 6a). As in Zhang et al. (2003), the DTE is defined as

$$DTE = \frac{1}{2} \sum [(\delta u)^2 + (\delta v)^2 + \kappa (\delta T)^2], \qquad (1)$$

where δu, δv, and δT are the difference wind components and difference temperature between two simula-

tions, $\kappa = C_p/T_r$, T_r is the reference temperature of 270 K, and i, j, and k run over x, y, and s grid points over one horizontal wavelength of the baroclinic waves estimated from the 30-km domain (the same as the 4200 km × 4200 km display domain used for Fig. 4).

As in TZRS04, the spectral density of the initial random perturbation (white noise added only to the temperature field) is proportional to the magnitude of the horizontal wavenumber vector (Fig. 6a). Despite a dramatic decrease of DTE at the smallest scales (<100 km; Fig. 6a) over the first 3 h owing largely to model diffusion (see Snyder et al. 2003; TZRS04; Zhang et al. 2006), the domain-integrated DTE increases significantly (Fig. 5), particularly at scales ~150–200 km. Figure 6a shows that the saturation of the error spectrum at scales smaller than 200 km is complete by 6 h and that the error growth rate at intermediate scales (200 km < L < 1000 km) decreases between 12 and 18 h. Consistent with the visual impression from the error
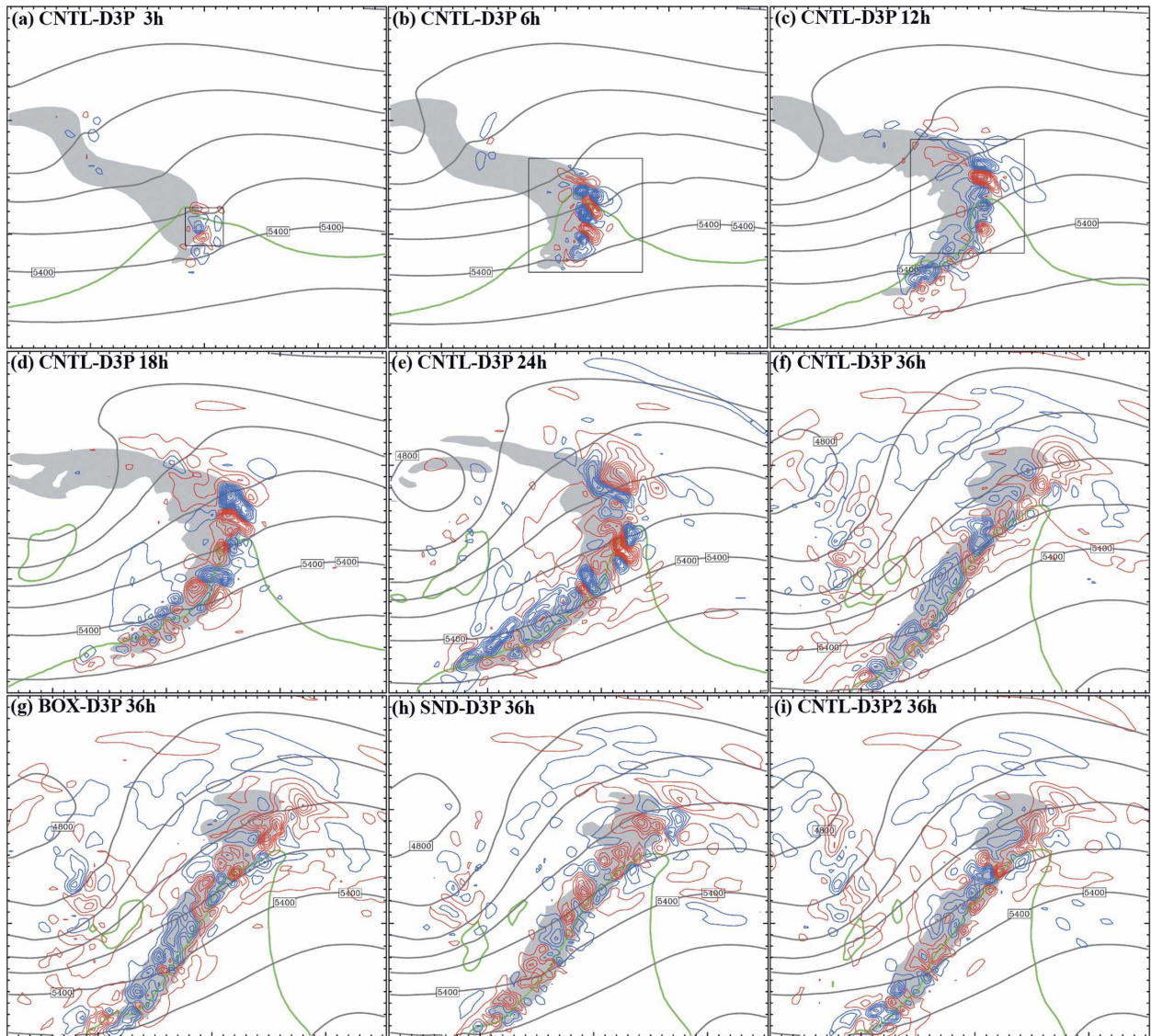
FIG. 4. The 500-hPa meridional wind difference (thin lines; $\Delta = 2$ m s^{-1}; positive, red; negative, blue) between CNTL-D3 and CNTL-D3P valid at (a) 3, (b) 6, (c) 12, (d) 18, (e) 24, and (f) 36 h of the nested-domains simulation plotted on a subdomain of D2. The 500-hPa geopotential height (dark solid; $\Delta = 120$ dam), the 3-h accumulated precipitation (>3 mm shaded), and the CAPE of 50 J kg^{-1} m^{-1} (green lines) in CNTL-D3P are also plotted. The distance between small tick marks is 90 km. The square boxes in (a)–(c) denote the locations of the display domains in Figs. 8–10. (g)–(i) As in (f) except for difference between (g) BOX-D3P and CNTL-D3, (h) SND-D3P and CNTL-D3, and (i) CNTL-D3P1 and CNTL-D3P2 valid at 36 h.

field shown in Fig. 4, Fig. 5 shows that the DTE continues to grow after 18 h, but at a still smaller rate; Fig. 6a shows that this later growth is associated with larger wavelengths ($L > 1000$ km). Figure 6a further shows that over the same period, the peak of the spectrum gradually migrates with time to intermediate scales (500–1000 km) as both the scale of variation of the wind differences and their areal extent increase (Figs. 4e–f). Figure 6b will be discussed below in relation to a special test case.

Figure 7 shows the time evolution of the DTE at three characteristic scales: the smaller-scale component with horizontal wavelengths less than 200 km, the intermediate-scale component between 200 and 1000 km, and the large-scale component with wavelength greater than 1000 km. Consistent with Fig. 6a, the DTE growth at scales smaller than 200 km slows down significantly after 6 h and the DTE growth at scales between 200 and 1000 km slows down after 15 h. After 12–18 h, most of the DTE power resides at the intermediate (meso-)
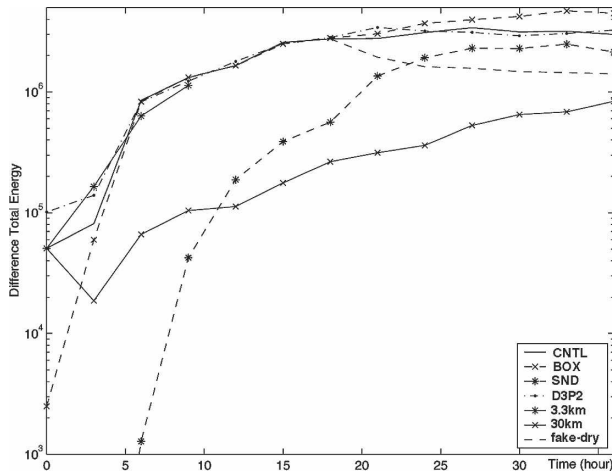
FIG. 5. Evolution of DTE ($m^2 s^{-2}$) integrated over a horizontal wavelength of the baroclinic wave estimated on the 30-km grid in experiments with different model resolutions (i.e., CNTL 10 km, solid; 30 km, solid with "×"; 3.3 km, solid with "*") and initial perturbations (i.e., BOX-D3P, dashed with "×"; SND-D3P, dashed with "*"; CNTL-D3P2, dotted–dashed) and between the two fake-dry simulations (dashed).

scales (200 km, 1000 km). Selection of the cutoff wavelengths between the three scales is rather arbitrary but the conclusions reached herein are not particularly sensitive to this choice.

The variation of difference growth with scale shown in Fig. 7 fits with the Lorenz (1969) picture of a system with a finite, intrinsic limit of predictability. Differences grow at the smallest (resolved) scale, where they saturate at relatively small amplitude. Differences at increasingly larger scales grow more and more slowly, but attain larger and larger amplitudes. The predictability of the largest scales is then limited by the rapid growth of differences at smaller scales.

In the present convection-permitting simulations, the differences grow and spread upscale in a manner that is qualitatively similar to that found in TZRS04 in its scale dependence (cf. Fig. 6a with Fig. 6 of TZRS04) but quantitatively much faster than those in the 30-km simulations of TZRS04 with parameterized convection (solid red curve with × symbols in Fig. 5). Much stronger error growth in the high-resolution convection-permitting experiments than the lower-resolution experiments was also found in Zhang et al. (2003) for the "surprise" snowstorm. This raises the question of how the present results would be changed with further increases of resolution.

Figure 5 shows that changing the horizontal grid increments from 10 to 3.3 km leads to a larger error growth rate in the first 3 h. Spectrum analysis of the 3.3-km simulations (not shown) indicates that these

smaller-scale, faster-growing errors saturate after 3 h and hence the error at 9 h using the 3.3-km grid is only slightly smaller than it is on the 10-km grid. This behavior is again consistent with a system having finite intrinsic predictability. Moreover, going to higher resolution does not introduce qualitatively new dynamics nor is the difference growth significantly more rapid after the first 3 h. Hence for the remainder of this paper we concentrate on the 10-km convection-permitting simulations that appear to represent marginally well the mesoscale aspects of moist convection and thus can be used to identify the error-growth dynamics for the simulated moist baroclinic waves in this study.

5. A three-stage error-growth conceptual model

The convection-permitting experiments in the previous section demonstrated that small-scale smallamplitude initial errors could grow rapidly and spread upscale in the present simulations of moist baroclinic waves. A closer examination of the difference between the two 10-km simulations (CNTL-D3 and CNTL-D3P) discussed below suggests three distinct stages of error growth.

a. Stage 1: Convective instability and saturation (0–6 h)

Figure 8 shows the differences of vertical velocity w and temperature T at 500 hPa between CNTL-D3 and CNTL-D3P valid at 3 h of the nested domain simulations in a 300-km square box indicated in Fig. 4a, where the maximum 500-hPa wind difference v occurs. Examination of the differences of the total hydrometeor mixing ratio (q_{rc}) (which includes cloud and precipitable water/ice; not shown) reveals that this is also the area of significant difference in moist processes. Differences in all fields grow in the area of strong moist convection indicated by a high value of CAPE and heavy precipitation (Figs. 4a,b) collocated with significant q_{rc} differences. The 500-hPa T (w) difference grows from an initial magnitude of 0.2 K (0 m s^{-1}) to a maximum of ~3 K (~7 m s^{-1}) at 3 h (Fig. 8) and ~7 K (~13 m s^{-1}) at 6 h (not shown). The differences of w are also comparable to the maximum values found in either CNTL-D3 or CNTL-D3P at these times (3–6 h), indicating complete displacements of intense individual convective cells between the unperturbed and perturbed simulations. Such displacements also imply local error saturation at the convective scales, consistent with the v-wind difference (Figs. 4a,b) and the evolution of DTE at scales below 200 km (Fig. 7) described above. Moreover, maximum differences of q_{rc}, w, and T are mostly
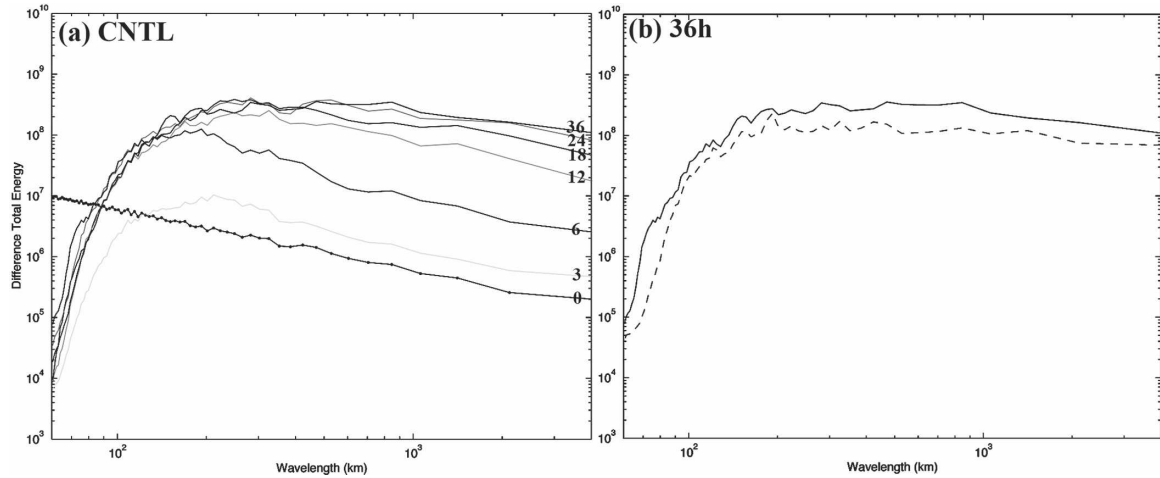
FIG. 6. (a) Power spectra of the DTE ($m^2 s^{-2}$) between CNTL-D3 and CNTL-D3P plotted at 0, 3, 6, 12, 18, 24, and 36 h. (b) Power spectra of the DTE ($m^2 s^{-2}$) of experiments CNTL (solid) and CNTLfd (dashed) at 36 h.

positively correlated along the line of strongest convection (warm updrafts with higher q_{rc} and cold downdrafts with lower q_{rc}; not shown) further indicating the significance of moist convection and the associated diabatic heating in forcing the differences (which will become more evident in the difference energy budget analysis to be discussed in section 7).

The characteristic horizontal scales of the maximum differences along the convective line are 50–100 km or 5 to 10 times of the horizontal grid spacing (Fig. 8). These are the smallest resolved scales for the 10-km simulations and their excitation is typically a signal of moist convection in gridpoint numerical models.
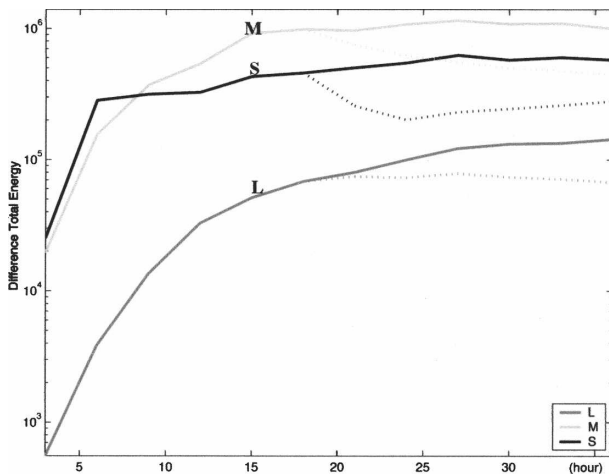
Slightly away from (especially ahead of) the maximum q_{rc} differences (not shown) and convective cells, the differences of w and T are nearly a quarter horizontal wavelength out of phase, which usually signals the propagation of smaller-scale gravity waves (Fig. 8). Vertically propagating gravity waves are also evident along the convective line but are mostly in the lower stratosphere above the top of the convective cells (not shown). The scales of these smaller gravity waves are also 50 ~ 100 km, consistent with spacing and displacement of the individual convective cells between the two
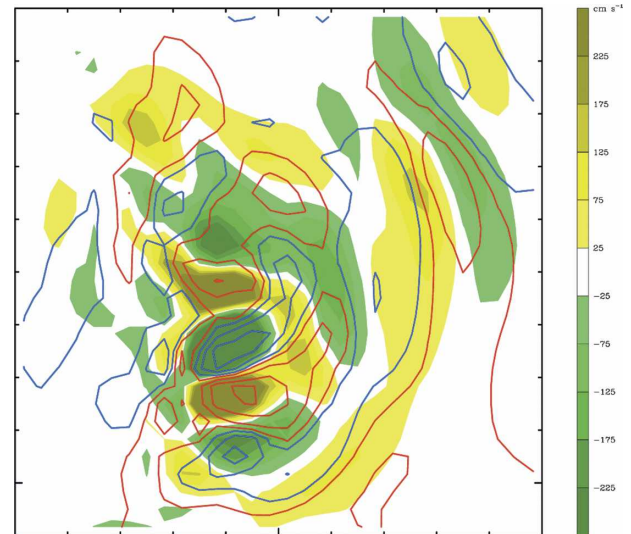

FIG. 7. Evolution of the domain-integrated DTE ($m^2 s^{-2}$) at three different characteristics scales (S: smaller-scale $L < 200$ km; M: intermediate-scale $200 < L < 1000$ km; and L: larger-scale $L > 1000$ km), between CNTL-D3 and CNTL-D3P (solid curves) and between CNTLfd-D3 and CNTLfd-D3P (dotted curves).

FIG. 8. The 500-hPa differences of vertical velocity (m s^{-1}, colored) and potential temperature [$\Delta = 0.2$ (1.0) K for values smaller (greater) than 0.5 (1.0) K; positive, red lines; negative, blue] at 3 h plotted on a subdomain of D3 (denoted in Fig. 4a). The distance between tick marks is 30 km.
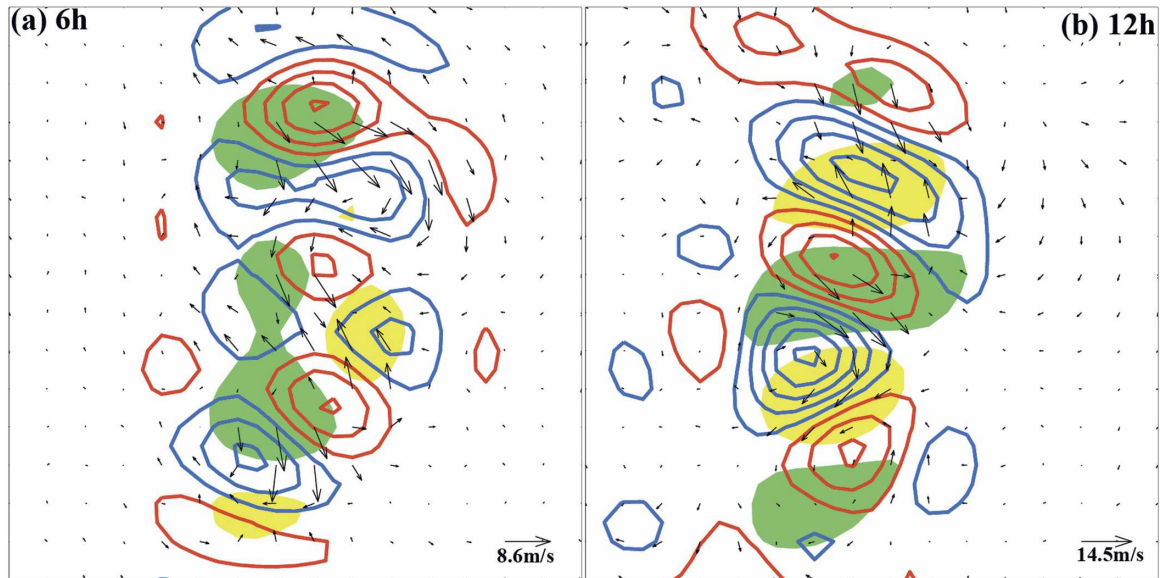
FIG. 9. The filtered differences valid at 6 and 12 h of 500-hPa potential vorticity ($\Delta = 0.2$ PVU; positive in red and negative in blue), total wind vectors (arrows plotted every 60 km), and total hydrometeor mixing ratio (>0.3 g kg^{-1} in yellow; <-0.2 g kg^{-1} in green). Signals with scales below 200 km are filtered out and the differences are plotted on a subdomain of D2 denoted in Figs. 4b,c.

simulations. These smaller scale gravity waves may disperse the error energy from the area of active moist convection.

Similar error-growth characteristics are also observed between CNTL-D4 and CNTL-D3 (Fig. 3d) as well as between CNTL-D4 and CNTL-D4P (error growth in the 3.3-km runs) interpolated to the 10-km grids at similar locations (not shown). The association of the initial error growth with conditional instability and moist convection was also found in Zhang et al. (2002, 2003), and TZRS04 and showed that moist convection is responsible for the rapid initial error growth in the simulations.

b. Stage 2: Transition and adjustment (3–18 h)

During the period when the difference error reaches saturation at the convective scales (3–6 h), differences in diabatic heating induce differences in potential vorticity that may affect the balanced motions. To identify the larger-scale error-growth processes the 2D spectral decomposition is used in Fig. 9 to filter out all signals with horizontal wavelength less than 200 km.

The maximum filtered 500-hPa potential vorticity (PV) difference, which is an indication of error in the balanced motions at the mesoscales, is greater than 0.7 PV units (PVU, where 1 PVU = 10^{-6} m^2 s^{-1} K kg^{-1}) at 6 h and 0.9 PVU at 12 h with horizontal wavelength of ~200–250 km at 6 h and ~250–350 km at 12 h (Fig. 9).

The maximum filtered pressure perturbation difference at 500 hPa (not shown) is negatively correlated with the maximum PV difference. The difference in the filtered horizontal wind vectors mostly rotates cyclonically around the maximum (positive) PV difference and anticyclonically around the minimum (negative) PV difference at similar scales. The relation of the PV differences to both the wind and pressure differences clearly indicates a substantial balanced response in the difference fields (Fig. 9).

Nevertheless, the correspondence between the PV differences and the wind and pressure differences is only partial, suggesting that a significant portion of the filtered horizontal wind differences is still unbalanced at these times. This conclusion is supported by the relative magnitudes of the filtered horizontal divergence and vertical vorticity, which we take to be a crude measure of the degree of balance in the differences. The maximum amplitude of the filtered horizontal divergence (relative vorticity) is 11.1 (14.4) $\times$ 10^{-5} m^{-1} at 6 h and 17.3 (24.2) $\times$ 10^{-5} m^{-1} at 12 h. Figure 10 shows the ratio of the domain-averaged root-mean-square (RMS) difference of the filtered horizontal divergence divided by the RMS difference of the filtered relative vorticity. This ratio evolves from much larger than unity at earlier times to a near-constant value less than 1. Figure 10 further demonstrates the growth of the balanced component of the differences during the first 12 h, although the unbalanced component remains
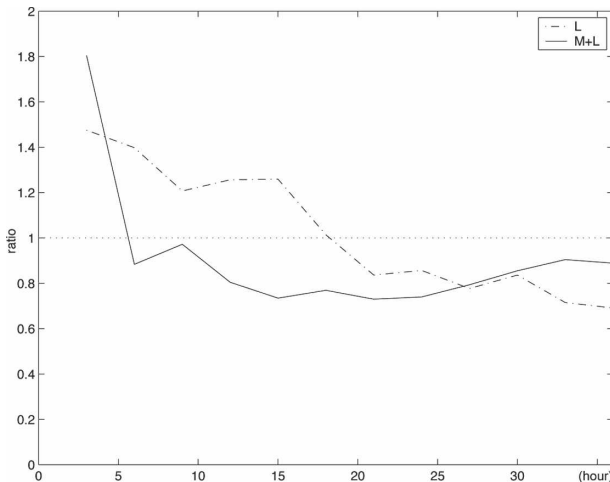
FIG. 10. Evolution of the ratio of the domain-averaged RMS difference of the filtered horizontal divergence over that of the filtered relative vorticity. The solid (dotted–dashed) curve is from signals with scales below 200 (1000) km filtered out.

comparable to the balanced component at the intermediate scales through the remainder of the simulation.

By 12 h, the differences have a distinct organization following the cold front of the baroclinic wave (Fig. 9b). The differences in all the fields alternate in sign along the front with a wavelength of roughly 300 km, which is much larger than the scale of the differences associated with individual convective cells and is consistent with Fig. 6a. The alongfront organization extends into other variables, such as rainwater (green and yellow shading) and temperature (not shown). Away from the front, the differences reflect propagating mesoscale gravity waves as can be seen from the significant values of the wind vectors away from the PV maxima and minima associated with the convective line (e.g., upper right corner of Fig. 9b). The present experiments do not fully elucidate the mechanisms responsible for the growth, scale, and organization of the differences, although possibilities include gravity waves produced by convective heating followed by geostrophic adjustment (e.g., Chagnon and Bannon 2005), growth of diabatic Rossby vortices (e.g., Moore and Montgomery 2005), cold pools at low levels (which are present near many of the convective cells), and instabilities of the front itself. We will show in sections 6 and 7, however, that latent heat release remains central to the difference growth at this stage.

c. Stage 3: Large-scale baroclinic growth (beyond 12 h)

At the final stage of the error growth, the error from the transitional stage that is carried by the balanced motion may subsequently grow with the large-scale

baroclinic instability. This final phase of error growth toward larger scales depends strongly on the evolution of the background baroclinic waves and, as shown in Fig. 7, is slower than those of convective growth and geostrophic adjustment in stages 1 and 2. To illustrate the error-growth behavior for the balanced, larger-scale fields, the 2D spectral decomposition is again used. Signals with horizontal wavelengths smaller than 1000 km are filtered out.

Figure 11 shows the filtered 500-hPa differences of horizontal winds and perturbation pressure, over one horizontal wavelength (4200 km) of the background baroclinic waves at 12, 18, 24, and 36 h after the initial error was introduced. At 12 h, in addition to the balanced response in the smaller area of Fig. 9a described above, a pronounced negative pressure perturbation center of $\sim$0.3 hPa with an associated difference cyclonic circulation is induced to the southern trough region with a maximum wind difference greater than 0.5 m s^{-1} downstream (Fig. 11a). The maximum larger-scale differences of negative pressure perturbation and winds increased to greater than 0.5 hPa and 1.5 m s^{-1} at 18 and 24 h (Figs. 11b,c). Significant reorganization and growth both in scale and magnitude of the difference circulation occur at subsequent times. At 36 h, there is a positive pressure perturbation difference with maximum greater than 0.7 hPa in the trough and a nearly equal amplitude negative difference in the ridge (Fig. 11d), and the scale of the differences is comparable to that of the baroclinic wave.

The above result demonstrates that, after three different stages of error growth starting from moist convection, the small-amplitude, purely random noise can have a noticeable impact on the forecast of moist baroclinic waves on the time scale of $O(1$ day$)$. The amplitude of the larger-scale ($>$1000 km) differences is comparable to the differences between observations and 6–12-h forecasts from global numerical weather prediction models and to the initial perturbations used by Zhu and Thorpe (2006), which are expected to grow subsequently with the baroclinic waves and to limit the synoptic-scale forecast on the time of $O(5$ days$)$. The synoptic predictability at the medium range (longer than 1–2 days) is beyond the scope of the current investigation. The upscale growth of localized PV perturbations with the background baroclinic waves was also examined in Beare et al. (2003) and Gray (2001).

Note that the characteristic physical processes of different stages of error growth can coexist at the same time. For example, during the final phase of the balanced error growth, the adjustment of diabatic heating energy through inertia gravity waves persists and the unbalanced response remains a significant portion of
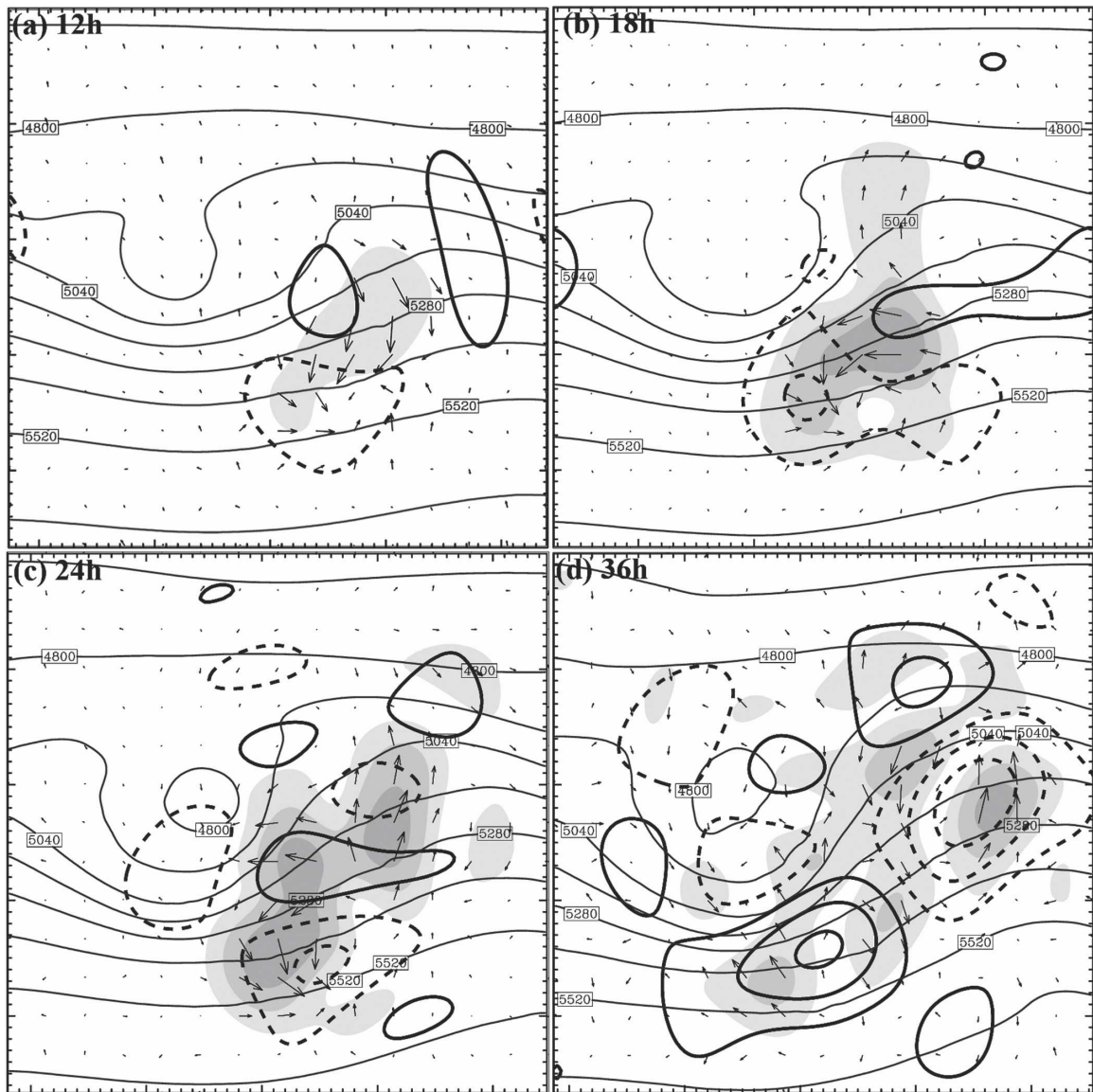
FIG. 11. The filtered differences of the 500-hPa perturbation pressure (thick lines; $\Delta = 0.2$ hPa; negative, dashed) and total wind vectors (arrows with values greater than 0.5 shaded every 0.5 m s^{-1}) along with the 500-hPa geopotential height from CNTL-D3P (thin lines, $\Delta = 120$ dam) valid at (a) 12, (b) 18, (c) 24, and (d) 36 h. All signals with scales below 1000 km are filtered off and the differences are plotted on a subdomain of D2. The distance between small tick marks is 90 km.

the total difference (Fig. 10). The difference in the inertia–gravity wave response (stage 2) may also trigger rapid error growth due to convective instability in the far field (stage 1).

6. Sensitivity to initial perturbations and moisture contents

The previous sections showed that the initial random perturbations between CNTL-D3 (unperturbed) and CNTL-D3P (perturbed) experiments decayed every-

where except for a small region in the southeast quadrant of the upper-level trough and surface cyclone where there is strong CAPE and sufficient low-level lifting. The significance of the rapid initial error growth in this small region of convective/conditional instability becomes even more obvious in experiment "BOX-D3P," which uses exactly the same perturbations as in CNTL-D3P but the perturbations are only applied only to the small shaded rectangular box of high CAPE denoted in Fig. 1.

The evolution of the difference between CNTL-D3

and BOX-D3P undergoes virtually the same multistage error growth as described above. For example, the 500-hPa v-wind difference at 36 h (Fig. 4g) is comparable in horizontal extent, scale, and magnitude to that between CNTL-D3 and CNTL-D3P (Fig. 4f). In terms of domain-integrated DTE (Fig. 5, dotted curve with "×"), despite a much smaller initial difference (less than 5%), the DTE error between BOX-D3P and CNTL-D3 grows to an amplitude comparable to that between CNTL-D3P and CNTL-D3 over the first 3 h and becomes even slightly larger at 21 h with the trend continued to 36 h. Experiment BOX-D3P further demonstrates that the effective error growth (between CNTL-D3 and CNTL-D3P) over the first 3 h is much stronger than estimated from the domain-integrated DTE alone. Rapid error growth due to moist convection occurs initially over the region of strong convective/conditional instability. This is also true even if we only perturbed one vertical column of the model grid (i.e., vertical sounding) inside the unstable region as in experiment "SND-D3P."

The difference between CNTL-D3 and SND-D3P triggers a displacement of a convective cell at the very beginning (not shown). Despite a 3–6-h delay of error saturation at the convective scales (suggested from DTE in Fig. 5), the 500-hPa v-wind difference (Fig. 4h) and the DTE at 36 h (Fig. 5) between CNTL-D3 and BOX-D3P are again comparable in horizontal extent, scale, and magnitude to that between CNTL-D3 and CNTL-D3P (Fig. 4f). Similar evolution of the difference field is also found between two perturbed experiments, that is, CNTL-D3P and another perturbed experiment, CNTL-D3P2, which is the same as in CNTL-D3P but with a different realization of random perturbations (Fig. 4i and dotted–dashed curve in Fig. 5).

We also examined the effects of initial moisture distribution on mesoscale predictability with convection-permitting simulations, in which the initial relative humidity of domain D1 is reduced to 70%, 40%, and 0% of that in CNTL, for both perturbed and unperturbed sets of simulations. The same perturbations used for CNTL-D3P are used in the perturbed simulations. From both the v-wind difference and the domain-integrated DTE, significantly and decreasingly smaller error growth is found in these experiments with decreasingly less moisture contents (not shown). The smaller difference with less moisture content occurs at all scales at 36 h compared to those between CNTL-D3 and CNTL-D3P at this time (not shown). Consistent with TZRS04, since the simulations with larger relative humidity exhibit greater conditional instability and stronger moist convection, the relation between initial

humidity and error growth also supports our assertion that the moist convection controls the initial phase of the error growth.

The aforementioned experiments and those from TZRS04 and Zhang et al. (2003) further demonstrate that moist convection is essential in organizing and amplifying small-scale small-amplitude disturbances over the first 3–6 h of the simulations. One may ask whether convection (or moist processes) is necessary to sustain the error growth after the difference energy has already grown and spread to larger scales. An additional pair of experiments ("CNTLfd-D3" and "CNTLfd-D3P") is performed in a manner similar to CNTL except that, after 18 h of the nested domain integration, latent heating/cooling from moist processes is turned off in both the perturbed and unperturbed runs. The subsequent DTE evolution from CNTLfd is plotted in dashed curve of Fig. 5, from which one can see that the DTE drops quickly and reduces to about half of its moist counterpart after another 18 h of "fake dry" integration. The result from the "fake dry" experiment further demonstrates fundamental differences exist between dry and moist simulations in terms of mesoscale predictability.

The result from the present 10-km fake-dry simulations, however, is in strong contrast to the 30-km experiments with parameterized convection of TZRS04, in which the DTE drops by an order of magnitude after the turning off of latent heating (Fig. 11 of TZRS04). At the beginning of the fake-dry runs (18 h), the present 10-km experiment has a significantly larger portion of error (difference) at the larger scales (>1000 km; Fig. 5) than that in TZRS04 (their Fig. 6). Since the larger-scale difference is less affected by dissipation, it can retain much of its amplitude while evolving with the background baroclinic waves. The dotted curves in Fig. 6b show that reduction of the DTE error in the fake-dry simulations comes from all scales but most dramatically at smaller scales. For example, the 500-hPa v-wind differences from the fake-dry simulations at 24 and 36 h (Fig. 12) has a much smaller, localized, smaller-scale maxima than those of CNTL (Figs. 4e,f), but the differences of the filtered large scale (>1000 km) of the 500-hPa pressure perturbation and winds in the fake-dry runs (Fig. 13) are comparable in magnitude to those of CNTL (Figs. 11c,d). Noticeably, the larger-scale (and more balanced) differences between CNTLfd simulations are similar in structure to those of CNTL at 24 h (Fig. 11c versus Fig. 13a) but they evolved into a significantly different larger-scale pattern at 36 h (Fig. 11d versus Fig. 13b), indicating that the error growth at stage 3 may also be significantly modulated by moist dynamics.
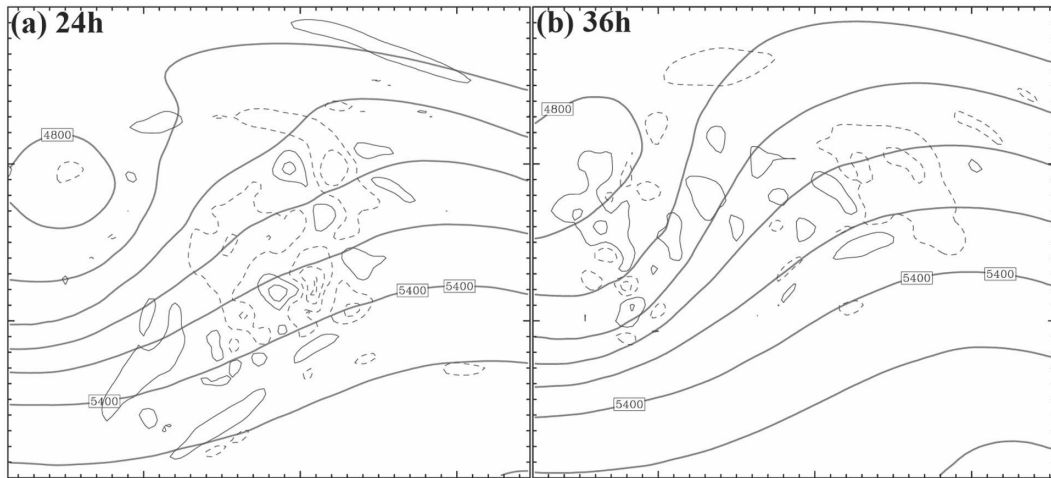
FIG. 12. As in Figs. 4e,f except for CNTLfd without precipitation valid at (a) 24 and (b) 36 h.

7. Budget analysis of difference kinetic energy

To further quantify the impacts of moist convection and other physical processes on mesoscale predictability, a budget analysis of the difference kinetic energy (DKE) between the perturbed and unperturbed experiments is performed. The breakdown of the domain-integrated DKE tendency into different source and sink terms resembles closely the budget analysis of turbulent kinetic energy (TKE; Stull 1989; Holton 1992). The source and sink terms include buoyancy production or loss (which also includes hydrometer drag), nonlinear velocity advection (or shear production), redistribution, and net production by pressure gradient force, and dis-

sipation due to horizontal and vertical diffusions. The derivation of the DKE equation and the formulation and estimation of each term in the DKE budget are presented in the appendix.

The time evolution of the DKE tendency and each of the source/sink terms per area unit (i.e., integrated vertically) estimated with hourly model outputs from the 10-km grid of CNTL-D3 and CNTL-D3P is plotted in Fig. 14. Consistent with the DTE evolution plot in Fig. 5, maximum DKE tendency (growth rate) occurs during the convective phase of error growth (stage 1) and peaks at 4–5 h. A sharp decrease of the DKE growth from 5 to 7 h afterward coincides with the timing of convective-scale error saturation. During the adjust-
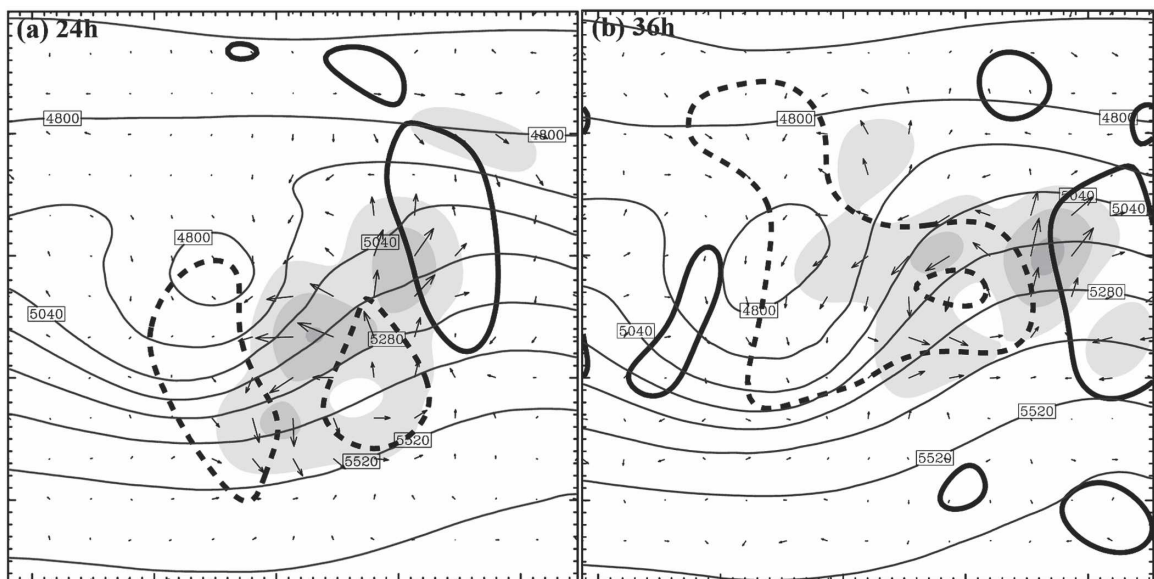

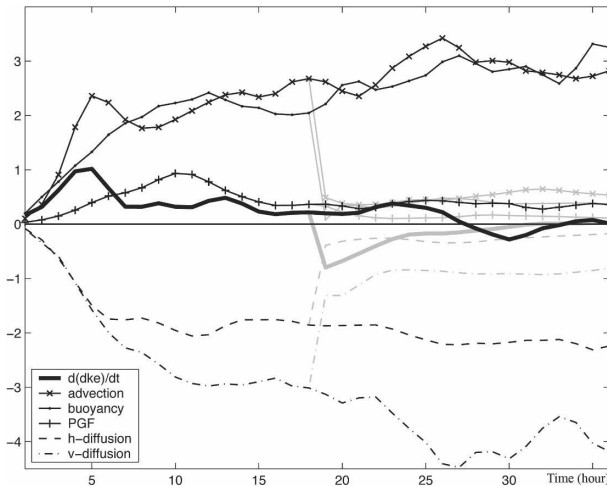FIG. 13. As in Figs. 10c,d except for CNTLfd valid at (a) 24 and (b) 36 h.

FIG. 14. Time evolution of the DKE tendency and each of the source/sink terms (J m^{-2} s^{-1}) estimated with the 10-km grid hourly outputs from CNTL-D3 and CNTL-D3P (solid) and from CNTLfd-D3 and CNTLfd-D3P (dashed).

ment period (7–12 h), the growth rate holds rather steady (stage 2). After a brief secondary maximum at 13 h, the DKE growth rate again falls considerably afterward. It becomes negative from 28 to 31 h but recovers to slightly positive for the final period of the simulation.

From the evolution of each term in the budget equation, it is found that buoyancy and nonlinear velocity advection are the two dominant source terms for error growth. These two terms are comparable in magnitude throughout the 36-h simulation. Further budget analysis of the thermodynamic equation (not shown) demonstrates that the buoyancy term comes primarily from diabatic heating due to moist convection. In other words, through warm updraft or cold downdraft (e.g., Fig. 8), the buoyancy term (i.e., vertical heat flux) redistributes diabatic heating from moist convection. The pressure force term is also positive but is less than 20% of the buoyancy or advection term. Except for the first few hours, these source terms are nearly balanced with the dissipation terms due to horizontal and vertical diffusion, which result in a small overall DKE growth (Fig. 3a).

The DKE budgets analysis is also performed for experiment CNTLfd (dotted curves in Fig. 14). As expected, the cessation of diabatic heating immediately leads to a dramatic decrease of buoyancy contribution (to less than 10% of its original magnitude). Moreover, the switching off of diabatic heating also leads to a sharp, immediate decrease in the nonlinear velocity advection (to less than 20% of its original magnitude). A relatively slower response (decrease) in the dissipation

terms leads to a large negative DKE tendency over the first few hours of the fake-dry simulations. The overall DKE tendency then equilibrates to nearly zero at 30 h. Budget analysis of the fake-dry experiment suggests that moist convection is not only crucial to the error growth in terms of buoyancy production, but it also leads to large shear production. In other words, numerous small but vigorous eddies due to moist convection can efficiently transport both heat and momentum and thus contribute to larger magnitude of both buoyancy production and nonlinear velocity advection in the DKE budget. It is worth noting that only nonlinear velocity advection is included in the error growth model of the pioneering predictability study of Lorenz (1969).

8. Summary and discussion

A recent study by the authors examined the predictability of an idealized baroclinic wave amplifying in a conditionally unstable atmosphere through numerical simulations with parameterized moist convection. It was demonstrated that with the effect of moisture included, the error starting from small random noise is characterized by upscale growth in the short term (0–36 h) forecast of a rapidly growing synoptic-scale disturbance. The current study seeks to further explore the mesoscale error-growth dynamics in the idealized moist baroclinic waves through convection-permitting experiments with model grid increments down to 3.3 km.

A multistage error-growth conceptual model is proposed. In the initial stage, the errors first grow from small-scale convective instability and then quickly saturate at the convective scales on time scales of $O(1 \text{ h})$. The amplitude of saturation errors may be a function of CAPE and its areal coverage determined by large-scale flows. In the transitional stage, the errors transform from convective-scale unbalanced motions to larger-scale balanced motions likely through geostrophic adjustment on the time scale of $O(1/f)$. Part of the errors due to difference in latent heating from convection may be retained in the balance fields while the others are radiating away in the form of gravity waves. In the final stage, the balanced components of the errors in the larger-scale flow grow with the background baroclinic instability. Though an examination of the difference-error energy budget, similar to the turbulence kinetic energy budget analysis, it is found that buoyancy production due mostly to moist convection is comparable to shear production due to nonlinear advection. Not only does turning off latent heating dramatically decrease buoyancy production, but it also reduces shear production (nonlinear velocity advection) to less than 20% of its original amplitude. These new findings fur-

ther demonstrate the effects of moist convection and diabatic heating on the limit of mesoscale predictability.

APPENDIX

The Difference Kinetic Energy Budget Equation

In an *f* plane without topography as used in our idealized simulations, the MM5 model is essentially using a height vertical coordinate and the momentum equations can be simplified as

$$\frac{\partial u}{\partial t} = -\mathbf{v} \cdot \boldsymbol{\nabla} u - \frac{1}{\rho}\frac{\partial p'}{\partial x} + fv + D_u, \tag{A1}$$

$$\frac{\partial v}{\partial t} = -\mathbf{v} \cdot \boldsymbol{\nabla} v - \frac{1}{\rho}\frac{\partial p'}{\partial y} - fu + D_v, \tag{A2}$$

$$\frac{\partial w}{\partial t} = -\mathbf{v} \cdot \boldsymbol{\nabla} w - \frac{1}{\rho}\frac{\partial p'}{\partial z} + \frac{\theta}{\theta_0} g - g(q_c + q_r) + D_w, \tag{A3}$$

where the last term of each equation represents the vertical and horizontal diffusion including vertical mixing due to the planetary boundary layer turbulence and/ or dry convective adjustment.

To investigate the evolution of difference kinetic energy between perturbed and unperturbed simulations, we subtract the above momentum equations from the corresponding momentum equation for the perturbed simulation that has the same form as the above equations, resulting in

$$\frac{\partial \delta u}{\partial t} = -\delta(\mathbf{v} \cdot \boldsymbol{\nabla} u) - \delta\left(\frac{1}{\rho}\frac{\partial p'}{\partial x}\right) + f\delta v + \delta D_u, \tag{A4}$$

$$\frac{\partial \delta v}{\partial t} = -\delta(\mathbf{v} \cdot \boldsymbol{\nabla} v) - \delta\left(\frac{1}{\rho}\frac{\partial p'}{\partial y}\right) - f\delta u + \delta D_v, \tag{A5}$$

$$\frac{\partial \delta w}{\partial t} = -\delta(\mathbf{v} \cdot \boldsymbol{\nabla} w) - \delta\left(\frac{1}{\rho}\frac{\partial p'}{\partial z}\right) + \frac{g}{\theta_0}\delta\theta - g(\delta q_c + \delta q_r)$$
$$+ \delta D_w. \tag{A6}$$

We further multiply Eqs. (A4)–(A6) by their respective momentum differences (i.e., $\rho_0\delta u$, $\rho_0\delta v$, and $\rho_0\delta w$) and the sum of the resulting equations can be expressed symbolically as follows:

$$\frac{\partial}{\partial t}(\text{DKE}) = \underbrace{-\rho_0[\delta u\delta(\mathbf{v} \cdot \boldsymbol{\nabla} u) + \delta v\delta(\mathbf{v} \cdot \boldsymbol{\nabla} v) + \delta w\delta(\mathbf{v} \cdot \boldsymbol{\nabla} w)]}_{\text{velocity advection/shear production term}} - \underbrace{\rho_0\left[\delta u\delta\left(\frac{1}{\rho}\frac{\partial p'}{\partial x}\right) + \delta v\delta\left(\frac{1}{\rho}\frac{\partial p'}{\partial y}\right) + \delta w\delta\left(\frac{1}{\rho}\frac{\partial p'}{\partial z}\right)\right]}_{\text{pressure gradient forcing term}}$$
$$+ \underbrace{\rho_0\left[\frac{g}{\theta_0}\delta w\delta\theta - g(\delta q_c + \delta q_r)w\right]}_{\text{buoyancy term (including hydrometer drag)}} + \underbrace{\rho_0[\delta u\delta D_u + \delta v\delta D_v]}_{\text{horizontal diffusion}} + \underbrace{\rho_0[\delta w\delta D_w]}_{\text{vertical diffusion}}, \tag{A7}$$

where the DKE is defined as

$$\text{DKE} = \frac{\rho_0}{2}[(\delta u)^2 + (\delta v)^2 + (\delta w)^2]. \tag{A8}$$

REFERENCES

Anthes, R. A., Y. H. Kuo, D. P. Baumhefner, R. P. Errico, and T. W. Bettge, 1985: Predictability of mesoscale atmospheric motions. *Advances in Geophysics,* Vol. 28B, Academic Press, 159–202.

Beare, R. J., A. J. Thorpe, and A. A. White, 2003: The predictability of extratropical cyclones: Nonlinear sensitivity to potential vorticity perturbations. *Quart. J. Roy. Meteor. Soc.,* **129,** 219–237.

Boffetta, G., A. Celani, A. Crisanti, and A. Vulpiani, 1996: Predictability in two-dimensional decaying turbulence. *Phys. Fluids,* **9,** 724–734.

Bryan, G. H., J. C. Wyngaard, and J. M. Fritsch, 2003: Resolution

requirements for the simulation of deep moist convection. *Mon. Wea. Rev.,* **131,** 2394–2416.

Chagnon, J. M., and P. R. Bannon, 2005: Wave response during hydrostatic and geostrophic adjustment. Part I: Transient dynamics. *J. Atmos. Sci.,* **62,** 1311–1329.

Dudhia, J., 1993: A nonhydrostatic version of the Penn State–NCAR Mesoscale Model: Validation tests and simulation of an Atlantic cyclone and cold front. *Mon. Wea. Rev.,* **121,** 1493–1513.

Errico, R., and D. Baumhefner, 1987: Predictability experiments using a high-resolution limited-area model. *Mon. Wea. Rev.,* **115,** 488–504.

Gray, M. E. B., 2001: The impact of mesoscale convective-system potential-vorticity anomalies on numerical-weather-prediction forecasts. *Quart. J. Roy. Meteor. Soc.,* **127,** 73–88.

Grell, G. A., 1993: Prognostic evaluation of assumptions used by cumulus parameterizations. *Mon. Wea. Rev.,* **121,** 764–787.

Holton, J. R., 1992: *An Introduction to Dynamic Meteorology.* Academic Press, 511 pp.

Hong, S.-Y., and H.-L. Pan, 1996: Nonlocal boundary layer vertical diffusion in a medium-range forecast model. *Mon. Wea. Rev.,* **124,** 2322–2339.

Leith, C. E., 1971: Atmospheric predictability and two-dimensional turbulence. *J. Atmos. Sci.,* **28,** 145–161.

——, and R. H. Kraichnan, 1972: Predictability of turbulent flows. *J. Atmos. Sci.,* **29,** 1041–1058.

Lilly, D. K., 1972: Numerical simulation studies of two-dimensional turbulence. II. Stability and predictability studies. *Geophys. Astrophys. Fluid Dyn.,* **4,** 1–28.

Lorenz, E. N., 1969: The predictability of a flow which possesses many scales of motion. *Tellus,* **21,** 289–307.

Metais, O., and M. Lesieur, 1986: Statistical predictability of decaying turbulence. *J. Atmos. Sci.,* **43,** 857–870.

Moore, R. W., and M. T. Montgomery, 2005: Analysis of an idealized, three-dimensional diabatic rossby vortex: A coherent structure of the moist baroclinic atmosphere. *J. Atmos. Sci.,* **62,** 2703–2725.

Nuss, W. A., and D. K. Miller, 2001: Mesoscale predictability under various synoptic regimes. *Nonlinear Processes Geophys.,* **8,** 429–438.

Pielke, R. A., G. A. Dalu, J. S. Snook, T. J. Lee, and T. G. F. Kittel, 1991: Nonlinear influence of mesoscale land use on weather and climate. *J. Climate,* **4,** 1053–1069.

Rotunno, R., and J.-W. Bao, 1996: A case study of cyclogenesis using a model hierarch. *Mon. Wea. Rev.,* **124,** 1051–1066.

Shapiro, M. A., and Coauthors, 1999: A planetary-scale to mesoscale perspective of the life cycles of extratropical cyclones. *The Life Cycles of Extratropical Cyclones,* M. A. Shapiro and S. Gronas., Eds., Amer. Meteor. Soc., 1228–1251.

Snyder, C., T. M. Hamill, and S. B. Trier, 2003: Linear evolution of error covariances in a quasigeostrophic model. *Mon. Wea. Rev.,* **131,** 189–205.

Stull, R. B., 1989: *An Introduction to Boundary Layer Meteorology.* Kluwer, 680 pp.

Tan, Z.-M., F. Zhang, R. Rotunno, and C. Snyder, 2004: Mesoscale predictability of moist baroclinic waves: Experiments with parameterized convection. *J. Atmos. Sci.,* **61,** 1794–1804.

Vukicevic, T., and R. M. Errico, 1990: The influence of artificial and physical factors upon predictability estimates using a complex limited-area model. *Mon. Wea. Rev.,* **118,** 1460–1482.

Zhang, F., C. Snyder, and R. Rotunno, 2002: Mesoscale predictability of the "surprise" snowstorm of 24–25 January 2000. *Mon. Wea. Rev.,* **130,** 1617–1632.

——, ——, and ——, 2003: Effects of moist convection on mesoscale predictability. *J. Atmos. Sci.,* **60,** 1173–1185.

——, A. Odins, and J. W. Nielsen-Gammon, 2006: Mesoscale predictability of an extreme warm-season rainfall event. *Wea. Forecasting,* **21,** 149–166.

Zhu, H., and A. Thorpe, 2006: Predictability of extratropical cyclones: The influence of initial condition and model uncertainties. *J. Atmos. Sci.,* **63,** 1483–1497.